Received: 15 April 2020 | Revised: 22 August 2020 | Accepted: 24 August 2020

DOI: 10.1002/mrm.28520

FULL PAPER

Magnetic Resonance in Medicine

Accelerating in vivo fast spin echo high angular resolution diffusion imaging with an isotropic resolution in mice through compressed sensing

Maarten Naeyaert[1] | **Jan Aelterman**[2] | **Johan Van Audekerke**[1] | **Vladimir Golkov**[3] | **Daniel Cremers**[3] | **Aleksandra Pižurica**[2] | **Jan Sijbers**[4] | **Marleen Verhoye**[1]

[1]Bio-Imaging Lab, University of Antwerp, Antwerp, Belgium

[2]Imec-IPI, Department of Telecommunications and Information Processing, Ghent University, Ghent, Belgium

[3]Department of Computer Science, Technical University of Munich, Garching, Germany

[4]Imec-Vision Lab, University of Antwerp, Antwerp, Belgium

Correspondence
Maarten Naeyaert, Bio-Imaging Lab, University of Antwerp, Universiteitsplein 1, 2610 Wilrijk, Antwerp, Belgium.
Email: maartennaeyaert@hotmail.com

Funding information
Seventh Framework Programme, Grant/Award Number: FP7/2007-2013 and 27885; Herculesstichting, Grant/Award Number: AUHA/012 and HFSP RGP0006/201; Molecular Imaging of Brain Pathophysiology (BRAINPATH), Grant/Award Number: FP7-PEOPLE-2013-IAPP-612360; Bijzonder Onderzoeksfonds, Grant/Award Number: (ID) UA BOF-DOCPRO 2012

Purpose: Echo planar imaging (EPI) is commonly used to acquire the many volumes needed for high angular resolution diffusion Imaging (HARDI), posing a higher risk for artifacts, such as distortion and deformation. An alternative to EPI is fast spin echo (FSE) imaging, which has fewer artifacts but is inherently slower. The aim is to accelerate FSE such that a HARDI data set can be acquired in a time comparable to EPI using compressed sensing.

Methods: Compressed sensing was applied in either q-space or simultaneously in k-space and q-space, by undersampling the k-space in the phase-encoding direction or retrospectively eliminating diffusion directions for different degrees of undersampling. To test the replicability of the acquisition and reconstruction, brain data were acquired from six mice, and a numerical phantom experiment was performed. All HARDI data were analyzed individually using constrained spherical deconvolution, and the apparent fiber density and complexity metric were evaluated, together with whole-brain tractography.

Results: The apparent fiber density and complexity metric showed relatively minor differences when only q-space undersampling was used, but deteriorate when k-space undersampling was applied. Likewise, the tract density weighted image showed good results when only q-space undersampling was applied using 15 directions or more, but information was lost when fewer volumes or k-space undersampling were used.

Conclusion: It was found that acquiring 15 to 20 diffusion directions with a full k-space and reconstructed using compressed sensing could suffice for a replicable measurement of quantitative measures in mice, where areas near the sinuses and ear cavities are untainted by signal loss.

KEYWORDS
compressed sensing, diffusion, fast spin echo, HARDI, turbo spin echo

1 | INTRODUCTION

Higher order diffusion MRI uses models of diffusion that can give more insight into the local microstructure and fiber organization in a voxel and, therefore, has become prevalent in research. Examples of such models are high angular resolution diffusion imaging (HARDI),[1-3] and diffusion spectrum imaging (DSI).[4] Other models attempt to directly estimate the microstructure of the underlying tissue also outside of white matter, such as NODDI[5] and CHARMED,[6] SANDI[7] and CODIVIDE[8] (which uses spherical encoding), searching and testing appropriate models for diffusion-weighted MRI (DWI) data.[9,10] These higher order models require between 40 and 500 DWI volumes,[11] and hence, a long acquisition time. To accelerate the acquisition, DWI data are usually acquired using a spin-echo EPI sequence which is susceptible to image distortions due to eddy currents. Additionally, the long readout time and low bandwidth in the phase encoding direction makes the sequence sensitive to susceptibility artifacts, introducing further signal displacement, especially near cavities, such as the sinuses and ears.[12]

These artifacts can be avoided by using a fast spin echo sequence (FSE),[13,14] where multiple spin echoes are acquired within each repetition time (TR) to fill the k-space. The number of spin echoes generated per TR is called the echo-train length (ETL), and a higher ETL allows a faster acquisition. However, diffusion-weighted FSE (DW-FSE) measurements also suffer from several drawbacks. Most importantly, it is substantially slower as EPI, and the ETL is limited due to the fast signal decay caused by T_2 relaxation and the diffusion labeling. Multi-shot techniques are thus often used, especially at high b-values.

A second issue with DW-FSE is its sensitivity to phase errors, which leads to severe ghosting. These large phase shifts can be caused by motion during the diffusion sensitization phase, and violate the Carr-Purcell-Meiboom-Gill condition[15] in DW-FSE. A second problem is caused by slight errors in the slice excitation pulse or slice refocusing gradients, which produces a phase oscillation between the odd and even echoes.[16] Third, as with an EPI sequence, a multi-shot sequence may suffer from phase incoherencies between shots. Several techniques have been developed to tackle these three problems. For example, the multi-shot Cartesian FSE sequence developed by Mori and van Zijl[16] has proven to solve all three problems.

If the phase errors are corrected, DW-FSE sequences result in measurements of diffusion nearly untainted by inhomogeneity and distortion, but at the price of a longer acquisition time and a lower signal-to-noise ratio (SNR) compared to EPI acquisitions. DW-FSE has been applied in a clinical context in the spine[19] and oral cavities, which have tissue/air boundaries,[20] and in stroke.[21] It is occasionally used in preclinical settings[22] and ex vivo imaging.[23,24]

To reduce the acquisition time of DW-FSE diffusion to an acceptable level for single-shell HARDI acquisitions, compressed sensing (CS) can be used[25-27] to reconstruct data from incoherently undersampled data.

HARDI requires dense sampling of both k- and q-space and CS can either be used to reconstruct MRI images from undersampled k-space, to reconstruct the orientation distribution function (ODF) from undersampled q-space, or to reconstruct both from undersampled k- and q-space.

MRI images are compressible in wavelet bases,[28,29] and their extensions such as curvelets[30] and shearlets.[31,32] Minimization of the total variation has also been used as an extra condition.[33,34] CS undersampling schemes are usually "density-weighted," acquiring more data in the center compared to the edges of k-space.

Alternatively, undersampling can be applied in q-space, using fewer diffusion directions than conventionally needed to fit a diffusion model. An ODF or fiber orientation distribution function (FOD) can be modeled by a sparsifying transform, such as spherical ridgelets.[35] Michailovich et al[36,37] developed a method to apply CS on HARDI data, using spherical ridgelets to sparsely represent the ODF and total variation in the diffusion image space.

This work also focuses on the specific problems of preclinical research, and its need for replicable measurements. An example of this is constrained spherical deconvolution (CSD) analysis, which offers a broader framework for quantification, for example, for estimating the fiber density and cross-section[38] between populations, or for analysis of the connectivity.[39] Preclinical small-animal research routinely uses advanced MRI applications but is often inherently slower than clinical scanners. For instance, parallel imaging cannot be used due to the small coil size, while T_1 relaxation times are longer at high fields,[40] calling for a longer TR and thus, acquisition time.[41]

The goal of this study is to apply and investigate different strategies of CS to FSE HARDI acquisitions both on a numerical phantom and in in vivo mouse brains, with the aim to get replicable diffusion metrics at the speed of an EPI acquisition, that is, 20-25 min,[42,43] The strategies comprised undersampling in q-space alone, or combined q-space/k-space undersampling, using both data with a fully sampled k- and q-space, allowing for easy retrospective undersampling of the q-space and data, which was subsampled in q-space and mildly subsampled in k-space. Heavy EPI distortion artifacts associated with the often-higher main magnetic field make distortion correcting methods less effective. However, images need to be quantifiable and reproducible to be useful for scientific research. The apparent fiber density (AFD),[44] fiber complexity,[45] and tractography were analyzed, all derived from a CSD, rather than comparing, for example, the mean squared error of the data or FODs since there is no noiseless measurement that can be used as a valid standard. A viable

FSE sequence, would reduce the influence of inhomogeneity artifacts commonly found in certain brain regions when using EPI.

2 | METHODS

2.1 | FSE sequence

In our study, we used the double navigator technique as implemented by Mori and Van Zijl.[16] This sequence has previously been used at our institution,[22] but was modified in this work to allow different incoherent subsampling along the phase encoding direction for each volume. Their method uses variable crushers along the echo train[17] to dephase the stimulated echo component and suppress unwanted echoes, which results in a stable phase for both the odd and the even echoes. A phase oscillation between the odd and even echoes occurs in FSE-DWI due to imperfect refocusing pulses and for the phase difference between shots due to motion.[18] One odd and one even echo without phase encoding were used as navigators to estimate and correct this phase difference between the echoes in the same ETL, as well as those and between different shots. To preserve the signal at the high b-values used for HARDI acquisitions, an ETL of 4 echoes was used, excluding the two navigator echoes, which were placed at the end of the echo train. To reduce the signal loss due to T_2 relaxation, the 180° pulses within the ETL were spaced as closely together as possible.

2.2 | Compressed sensing

2.2.1 | Sampling and undersampling in q-space

The fully sampled single-shell HARDI data consisted of 60 diffusion directions on a whole sphere in q-space, determined by an electrostatic repulsion scheme,[46,47] using MRtrix 3.0_rc3.[48] Diffusion directions were ordered such that the q-space was filled as uniformly as possible upon truncation of the total scheme. Next, the q-space was retrospectively undersampled by selecting the n first diffusion volumes.[48] Five different subsets of the 60 directions were used, shown in Figure 1, consisting of 46 directions, 20 directions, 15 directions, 12 directions and 10 directions. A b value of 2500 s/mm^2 was employed for all acquisitions.

To reconstruct undersampled q-space data, an algorithm developed by Michailovich et al[36,37] was used. This algorithm uses 3D shearlets to reconstruct the ODF from a limited number of samples, enforcing sparsity within the measurements of a voxel. It enforces an additional total variation constraint over the image space of the shearlet components. The method

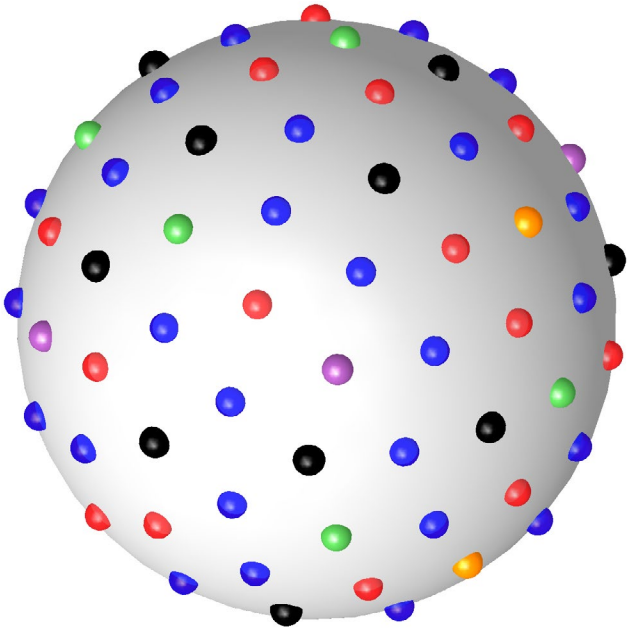

FIGURE 1 The q-space sampling scheme. The diffusion directions that were sampled with the different color-coded undersampling strategies. 10 directions = black, 12 directions = 10 directions + orange, 15 directions = 12 directions + purple, 20 directions = 15 directions + green, 46 directions = 20 directions + blue, 60 directions = 46 directions + red. Note that the directions are projected on a half-sphere here, but are recorded on a full sphere

was shown to perform very well in the SPArse Reconstruction Challenge (SPARC) at MICCAI in 2014.[49] Since a continuous ODF is constructed, new diffusion-weighted images can be resampled from the results.

2.2.2 | Undersampling in k-space

Undersampling in k-space is applied only in the phase-encoded direction, by randomly sampling a predetermined number of lines from a probability function for each volume. Phase encoding was done in the anterior-posterior (A-P) direction to reduce motion-like artifacts when undersampling the k-space. The sampling probability function is symmetrical around the center of k-space, with the sampling probability being 1 in a region around the center, and decreasing according to a power law in the periphery. In this work, 75% of k-space was sampled with 20% of the total k-space sampled fully in the center and a quadratic power law, which has been shown to result in images with an optimal reconstruction quality as measured using peak SNR in ex vivo FSE measurements.[50,51]

To reconstruct the images from undersampled k-space data, a SENSE-like[52] self-calibrating extension of the COMPASS algorithm is used.[53,54] Briefly, this method uses a split Bregman algorithm to apply L_1 regularization on the shearlet coefficients and total variation of the image.[31,32] Coil

sensitivity maps are estimated using the image of the fully sampled data of all the b_0 images and by promoting smoothness by using a finite differences operator in the regularization term.

2.3 | Phantom experiment

A phantom, 96 × 96 voxels, consisting of two straight fibers crossing at a 90° angle and a circular fiber intersecting both straight fibers was used, based on the developed by Michailovich et al. and described more in detail there.[36,37] In the crossings, one of the straight fibers has twice the intensity as the other fiber. The FSE sampling, both with and without k-space undersampling, was simulated using the same timing and sampling settings as for the in vivo experiments. T2 decay was simulated using a mono-exponential function using a T2 value of 45 ms for all fibers.[55] Rician noise was added to obtain SNR = 10. Sampling and subsampling of q-space was done as in the in vivo experiments. In addition, specific sets of 10, 12, 15, 20, and 46 directions were generated using MRtrix and used.

2.4 | Acquisitions

A total of six male black mice of 3 months old were scanned with a 7T Pharmascan scanner (Bruker, Ettlingen, Germany). A cross-coil setup was used with a quadrature volume coil for excitation and a 2 × 2-array mouse-head surface receiver coil. From all animals, we acquired a fully sampled k-space FSE HARDI acquisition consisting of 46 diffusion directions, within an acquisition time of 1 h 15 min, which was used as a standard. For two animals, the remaining 14 directions of the total scheme of 60 were acquired, which took about 22 min, but these were not acquired for all animals due to time constraints. For another three animals, data consisting of 20 directions and 75% of the total k-space, incoherently undersampled, was also acquired, which took about 22 min.

The acquisition parameters were: effective echo time (TE) = 22.5 ms, TR = 3000 ms, field of view (FOV) = (2.02 × 2.02) mm^2, resolution = (0.21 × 0.21) mm^2, matrix size (96 × 96), ETL = 4, read-out direction was left to right, and receiver bandwidth was 50 kHz. The whole brain was acquired using 33 horizontal slices with a slice thickness of 0.20 mm and an interslice distance of 0.21 mm. Bipolar trapezoid diffusion gradients were used, with $\delta = 4$ ms and $\Delta = 12$ ms, for b = 2500 s/mm^2. The first volume and every sixth volume thereafter was a b_0 image. The SNR of the raw data, calculated using the noise maps generated during the denoising step, was SNR = 4.18 ± 0.11.

The animals were brought under anesthesia using 3.5 % isoflurane (Abbott, Maidenhead, UK) with a 30% N_2/70% O_2 mixture at a flow rate of 600 ml/min and were kept under anesthesia using ~1.8% isoflurane during the scan. A breathing rate of ~120 breaths/min was maintained and measured using a pressure-sensitive pad. Body temperature was measured using a rectal probe and kept constant at (37.0 ± 0.2) °C using warm air and a feedback unit (SA Instruments, Stony Brook, NY, USA). Monitoring was done using PC-sam monitoring software (SA Instruments). All experimental procedures were performed following European guidelines (2010/63/EU) and were approved by the University of Antwerp Ethics Committee for Animal Experiments (approval number 2014-04).

2.5 | Image reconstruction and processing

A diagram of the workflow for preprocessing and processing is presented in Figure 2. Images were reconstructed from undersampled k-space data using the algorithm described in Section 2.2.2,[53] taking about 55 s/vol using a 3.40 GHz intel i7-3770 processor and matlab (The MathWorks, Natick, MA). Fully sampled k-space data were denoised by using redundancy in the data and identifying and removing the noise-containing principal components.[56,57] After subsequent image reconstruction, the FMRIB Software Library v6.0 (FSL)[58] was used to perform motion, eddy current artifact, and slice-wise-outlier detection and correction.[59,60] Data quality reports were generated[61] and data were checked visually to verify that no obvious artifacts, such as ghosting, were present. Diffusion directions were adapted according to the motion parameters.

The bias-field was estimated using the first b_0 image and applied to all volumes of the scan, using the N4ITK algorithm[62] implemented as part of the Advanced Normalisation Tools version 2.1.0 (ANTs).[63] A brain mask was drawn manually on the debiased b_0 image using Amira 5.4 (FEI Company, Hillsboro, OR, USA).

All data were reconstructed to 60 diffusion-weighted images (Figure 1), using the diffusion directions and CS reconstruction algorithm described above,[37] which took 100-200 s data set, depending on the number of directions used as input. Additionally, the data from the 46 directions was resampled to the same 60 directions using the same algorithm but without enforcing sparsity, and is referred to as "standard" acquisition in this work. Since no ground truth is known, the parameters of the algorithm cannot be trained to minimize the minimum squared error. In our experiments, we found that manual tuning to the point that no noise-induced or overfitting artifacts are perceivable yields satisfactory results and that the sensitivity of the result to the exact parameter setting is very low in this regime. This finding is reminiscent of the popular L-curve approach for parameter tuning.[64] Its significance is that a fixed set of parameters may be expected

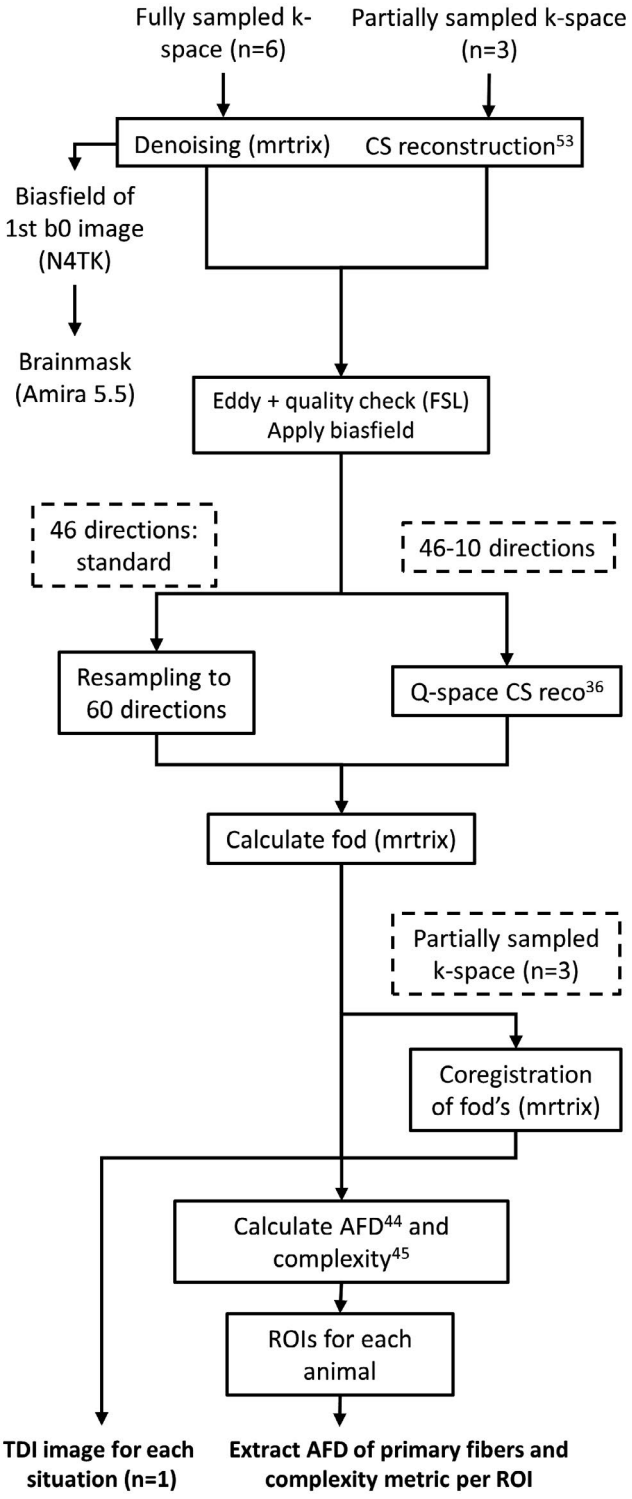

FIGURE 2 Schematic overview of the preprocessing and processing steps. Boxes with full lines indicate steps, boxes with dotted lines indicate on which data the step was executed, bold text indicates metrics used for evaluation

to give satisfactory results for data acquired under similar circumstances.

After preprocessing of the HARDI data, MRtrix 3.0_rc3[48] was used to perform CSD[1,2] and further analyze the data. The analysis is done for each subject separately, to investigate the replicability of the measurement. The fiber response function was estimated using the method of Tournier,[65] and FODs were estimated up to the 8th harmonic order.

2.6 | Quantitative ROI-based analysis

In the phantom, two single fiber ROIs were drawn, one containing a straight fiber and the other o-containing the circular fiber. ROIs were also drawn for the crossing of the two straight fibers, and for the crossing of the curved fiber with the straight fiber. The phantom and ROIs are shown in Figure 3.

For the in vivo data, seven ROIs were drawn on the "standard" image. Four single fiber ROIs were drawn, located in the posterior forceps of the corpus callosum (CC), the genu of the CC, the most ventral part of the optic tract, and the olfactory fiber. Furthermore, two crossing fiber regions were drawn, on the boundary between the CC and the fornix, and on the boundary of the CC and the cingulum. Last, a ROI was drawn in the somatosensory cortex, a gray matter area. All ROIs were drawn as defined in the Paxinos atlas (3rd edition).[66] The AFD[44] of the three primary fixels and complexity values per voxel[45] were calculated and averaged for each ROI. The AFD was calculated as the integral of the FOD lobe of a specific fixel, while the complexity represents the importance of the largest lobe within the entire FOD, and is a value between 0 (a single lobe) and 1 (all lobes are of equal importance). The FODs of k-space undersampled data were coregistered to the FODs of the fully sampled k-space,[67] and the fixel-fixel correspondence between the standard acquisition and every other acquisition strategy was determined for each animal.

2.7 | TDI images

For one of the subjects with both full and partial k-space acquisition, 5 000 000 tracts were traced for each reconstructed data set using the IFOD2 algorithm,[68] and the corresponding track density weighted images (TDI) at 1/10 of the original resolution were generated.[69]

3 | RESULTS

3.1 | Phantom analysis results

The results from the phantom experiment indicate that the AFD value of fixels with fibers decreases when fewer directions are used, while it increases for fixels without fibers. The variation becomes larger when fewer data are used.

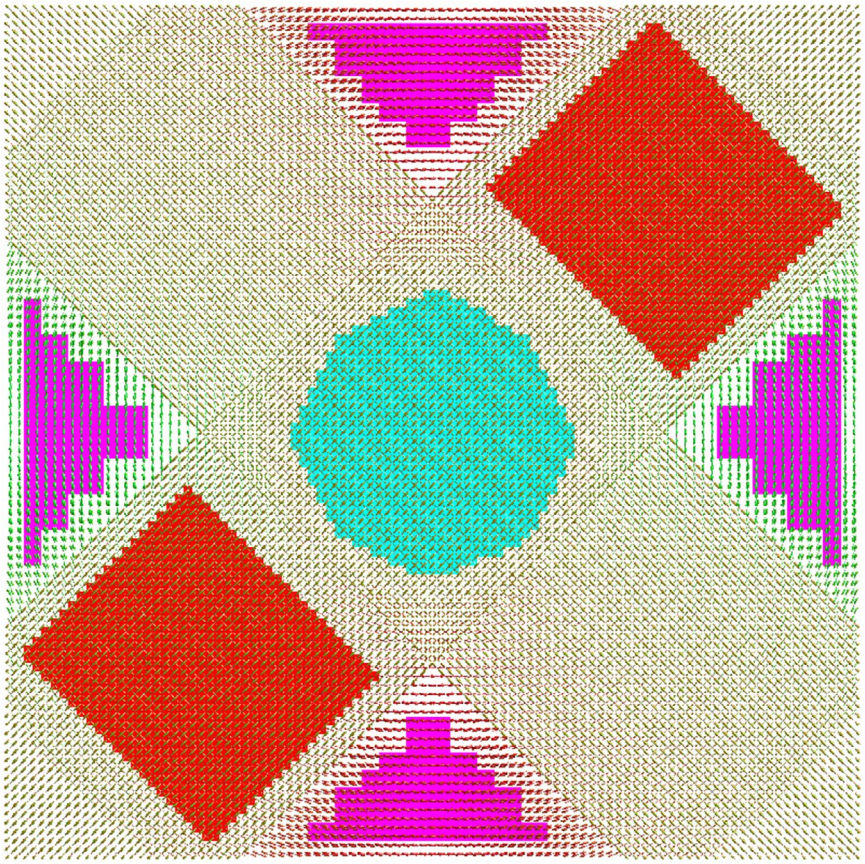

FIGURE 3 The phantom, which consisted of two straight fibers in a X configuration, and surrounded by a circular fiber. ROIs for the curved fiber (purple), crossing of the two straight fibers (blue) and the crossing of a straight and the curved fiber (red) are indicated. A different ROI for the straight fiber is not visible on this slice

However, the effect is smaller for the straight fiber ROIs (Figure 4A,C) as for those with a curved fiber (Figure 4B,D). In the crossing of the two straight fibers, the value of the primary fixels remains stable when using more as 12 directions while the tertiary fixel has a greater AFD value and variation. The crossing between the straight and curved fiber is affected the most by subsampling q-space, and has a lower AFD value for the two primary fixels but an increase of the AFD value of the tertiary AFD value and the variation.

The effect on the complexity measure is shown in Figure 4E, and generally shows an increase in the complexity of single fibers when fewer directions are used, and a decrease for the crossing fiber ROIs. The variation of the complexity measure increases when fewer directions are used. In all cases, undersampling of k-space has a negligible effect on the AFD and complexity metric.

A comparison of the AFD and complexity results between undersampling the 60 directions and using dedicated schemes with the desired number of directions are in Figure 5. It can be seen the dedicated q-space sampling schemes perform better in the ROIs with curved fibers (Figure 5B,D), but the primary fixel has lower AFD values in the ROIs with straight fibers (Figure 5A,C).

Results for additional noise levels are shown in Supporting Information Figure S1,which is available online, and generally show larger variations at lower SNR levels, and lower AFD values in actual fiber fixels for higher SNR when q-space subsampling is applied, while the tertiary fixel shows higher values.

3.2 | Visual inspection of b_0 images

An example of an average b_0 image of a fully sampled k-space, an undersampled k-space, and a fully sampled k-space without the phase correction is shown in Figure 6. Phase errors are visible when the correction is not applied (Figure 6A,D), as indicated with the red arrow. However, after the phase correcting step, these errors are substantially reduced (Figure 6B,E). For the images reconstructed from undersampled k-space data, some residual blurring remains. No deformation artifacts are visible in regions where these are typically observed when an EPI acquisition is employed, such as the olfactory bulb, and signal from regions deep in the brain is not lost (Figure 6D-F).

3.3 | ROI-based analysis

Figure 7 shows the average AFD value for the three principal fixels according to the standard acquisition, for both q-space undersampled experiments (Figure 7A) and combined k-space and q-space undersampling (Figure 7B). In single fiber regions (ie, posterior forceps and genu of the

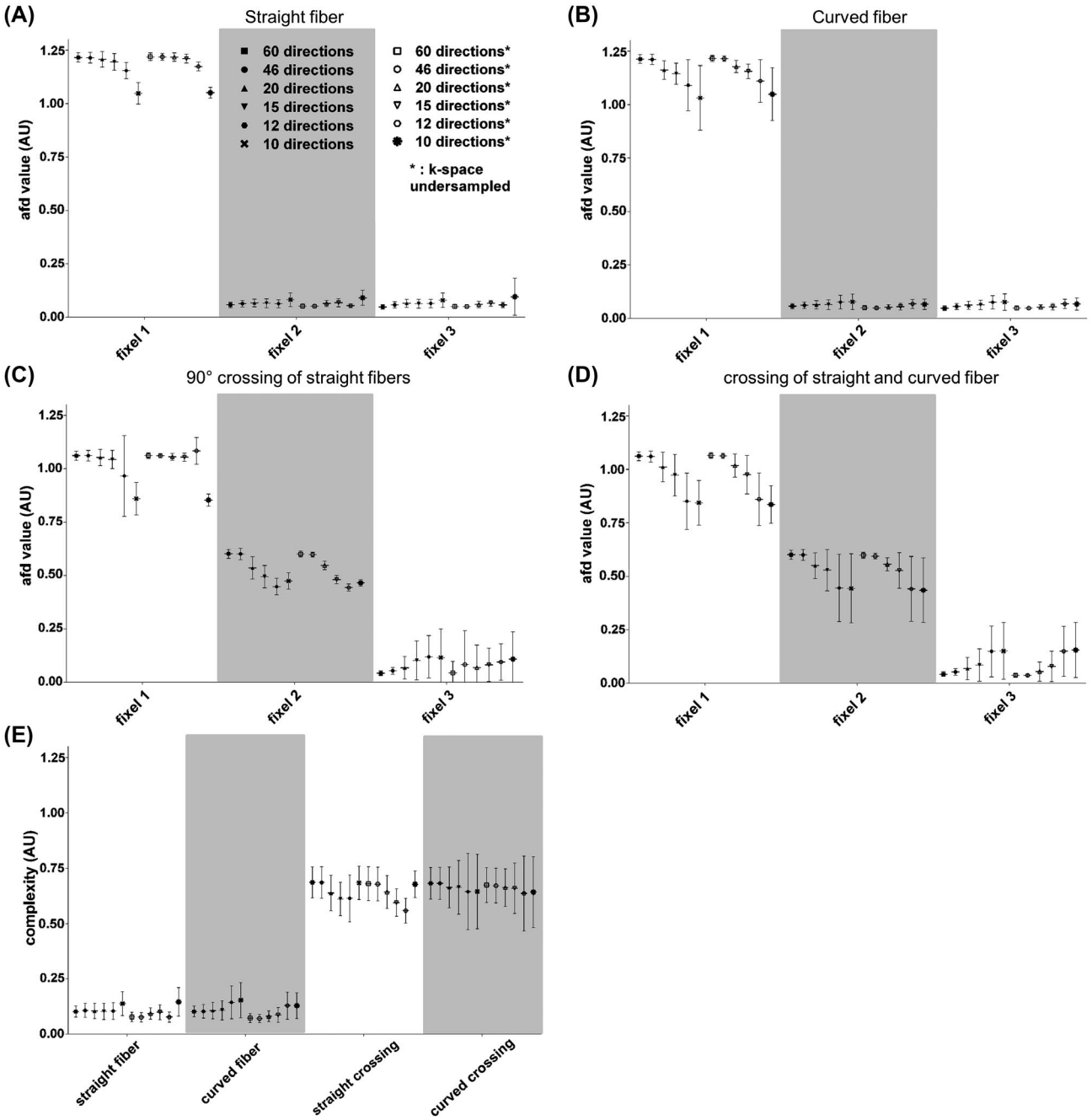

FIGURE 4 Results for all sampling strategies in the phantom, with SNR = 10. The AFD per fixel is shown for a straight fiber (A), a curved fiber (B), two straight fibers crossing at 90° (C), and a curved and straight fiber crossing (D). E shows the complexity metric for all four ROIs. Error bars indicate the SD over the ROI

CC, the optic tract, and the olfactory fiber), the secondary and tertiary lobes of the FOD have higher AFD values when fewer diffusion directions are used, though the effect is limited. AFD values of fibers that would be difficult to tract using an EPI sequence, such as those in the olfactory bulb and of the optic tract at the bottom of the brain, are well replicated and indicative of a single fiber. In the ROIs containing two important fibers, the AFD value of the tertiary lobe becomes higher when the number of diffusion directions used decreases, while the two main fibers remain of about equal importance. However, it should be noted that this tertiary lobe is not found in all voxels, and the data shown for this lobe is based on limited statistics. Finally, measures of the cortical ROI show only a slight increase in AFD when more undersampling is used. Overall, the data from the different acquisition strategies show a consistent change in the magnitude of the AFD and replicability.

The effect of additional k-space undersampling (Figure 7B) is similar but much larger. Increased q-space undersampling lowers AFD for all primary fixels of single fiber ROIs except

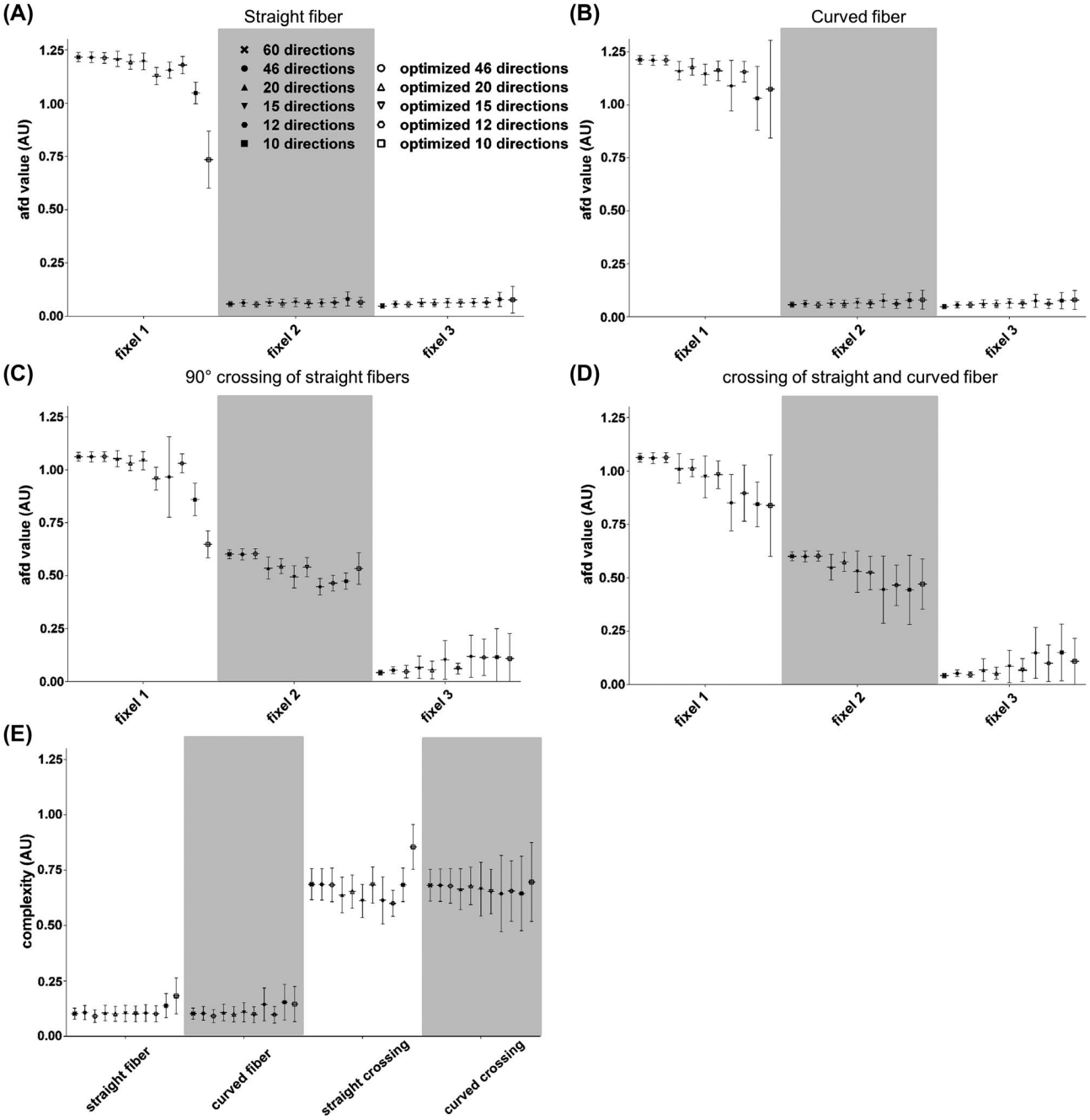

FIGURE 5 Results for subsampling from a diffusion table with 60 directions and diffusion tables with the desired number of directions, using a fully sampled k-space and SNR = 10. The AFD per fixel is shown for a straight fiber (A), a curved fiber (B), two straight fibers crossing at 90° (C), and a curved and straight fiber crossing (D). E shows the complexity metric for all four ROIs. Error bars indicate the SD over the ROI

the olfactory bulb, and increases AFD for secondary and tertiary fixels in all ROIs except the optic tract.

Figure 8 shows how the complexity measure responds to different degrees of undersampling for the ROIs. The complexity measure behaves as should be expected, with low values in single fiber regions, higher values when crossing fibers are present, and the highest complexity found in the cortex. The complexity metric remains very stable when only q-space undersampling is used (Figure 8A). Only for the very well-defined posterior forceps, undersampling q-space leads to an increase of the complexity measure and its group-based SD.

When combined with k-space undersampling (Figure 8B), the complexity is in general higher when less data are used for the single-fiber bundles, especially for the posterior forceps and the genu of the CC. The complexity remains stable in crossing-fiber regions and the somatosensory cortex.

3.4 | TDI images

The TDI results for a single representative animal are shown in Figure 9, for two levels in the brain. The top level

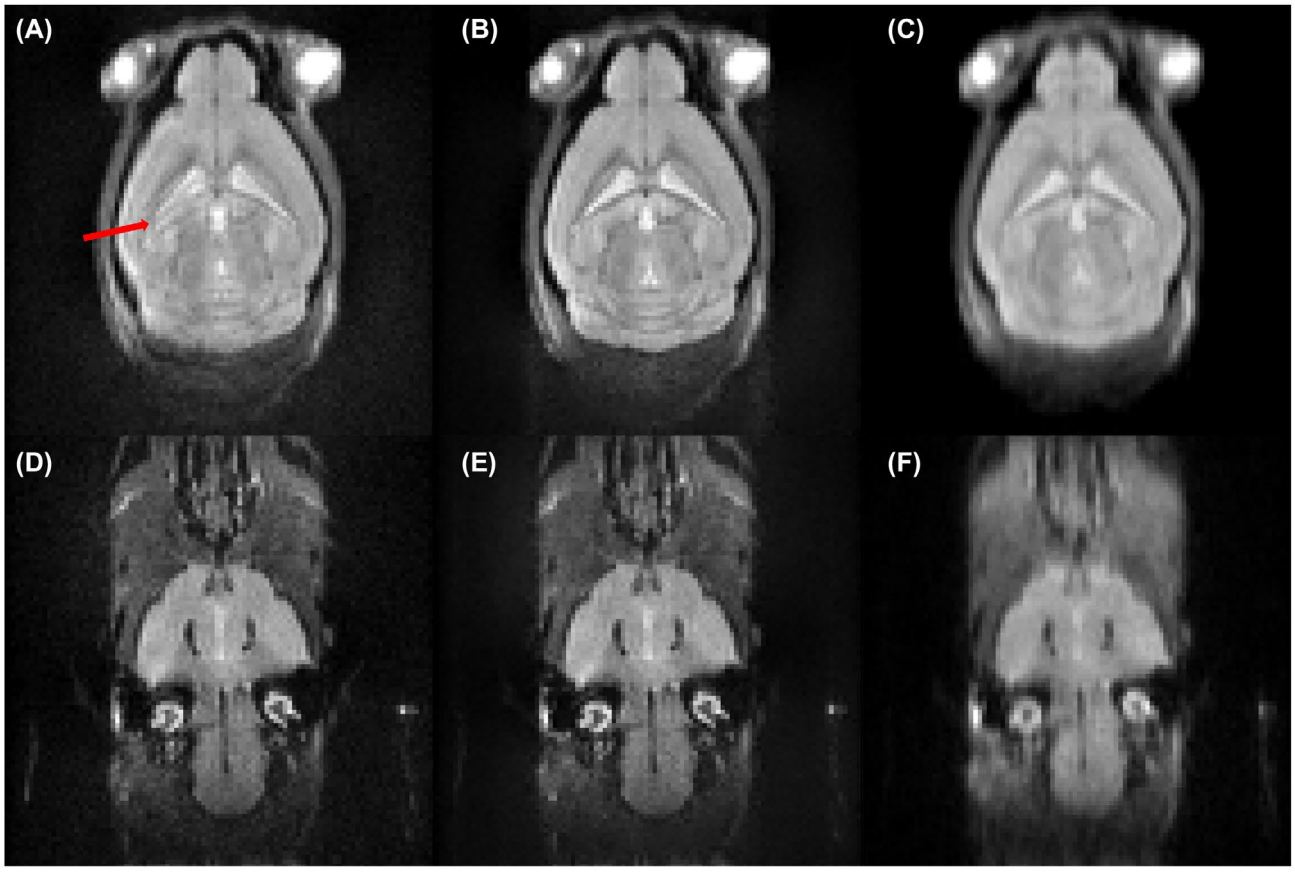

FIGURE 6 The b_0-images. Representative slices of a b_0 image of the FSE acquisition. A,D, Images from completely sampled k-space without the phase correction being applied. Ghosting is clearly present in A, for example, around the ventricles (red arrow). B,E, Full k-space image with phase correction applied, as used in the processing of the data. C,F, k-space undersampled image. No ghosting or incoherent artifacts are apparent, but the image is blurrier as a result of the undersampling in a single direction

(Figure 9A-J) is located near the dorsal edge of the lateral ventricles, which are clearly visible as black space between the CC, external capsula, and fornix. Caudal to this is the superior colliculus and cerebellum, with its laminar structure. The other level (Figure 9K-T) is at the interface of the dentate gyrus and habenular nuclei, which are shown in green on both sides of the 3rd ventricle and indicated with a white arrow on Figure 9K, and with the fimbria of the hippocampus just anterior of this. The fibers are quite well defined for the standard, 46 diffusion directions, and 20 directions. Using 15 directions, some degradation is visible (eg, Figure 9N, the right-hand side of the external capsula), which worsens when fewer data are used. For example, the brachia of the inferior colliculus, visible as blue lines running in the H-F direction just anterior of the cerebellum and indicated with a red arrow on Figure 9L can be clearly differentiated on images K-O but is less well defined in images P-T. The reconstructions from incomplete k-space data clearly demonstrate a lower quality (Figure 9G-J, Q-T), with fibers also present in the ventricles and no lamellar structure in the cerebellum, and the olfactory fibers not well defined. Only for the undersampled k-space and 20 directions (Figure 9G,Q), the ventricles and cortex remain relatively free of tracked fibers, and the important structures remain recognizable. Additional examples of TDI images, at the level of the anterior commissure and caudate putamen can be found in Supporting Information Figure S2.

4 | DISCUSSION

In this work, the combination of a DW-FSE sequence and CS was tested as a strategy to obtain HARDI data, which is almost free from deformation and inhomogeneity artifacts within a reasonable time frame and with an isotropic resolution. Undersampling for CS was applied either only in q-space or in k-space and q-space. Evaluation of the acquisition was done on a local scale by investigating several properties of the resulting FOD analysis in several ROIs, while evaluation on a macroscopic scale was done by constructing TDI images.

As shown in Figure 6, the phase correction reduces blurring and ghosting, and the olfactory bulb and regions deep in the brain near the ears are not affected by inhomogeneity artifacts (Figure 6B,E). While the crushers need to be

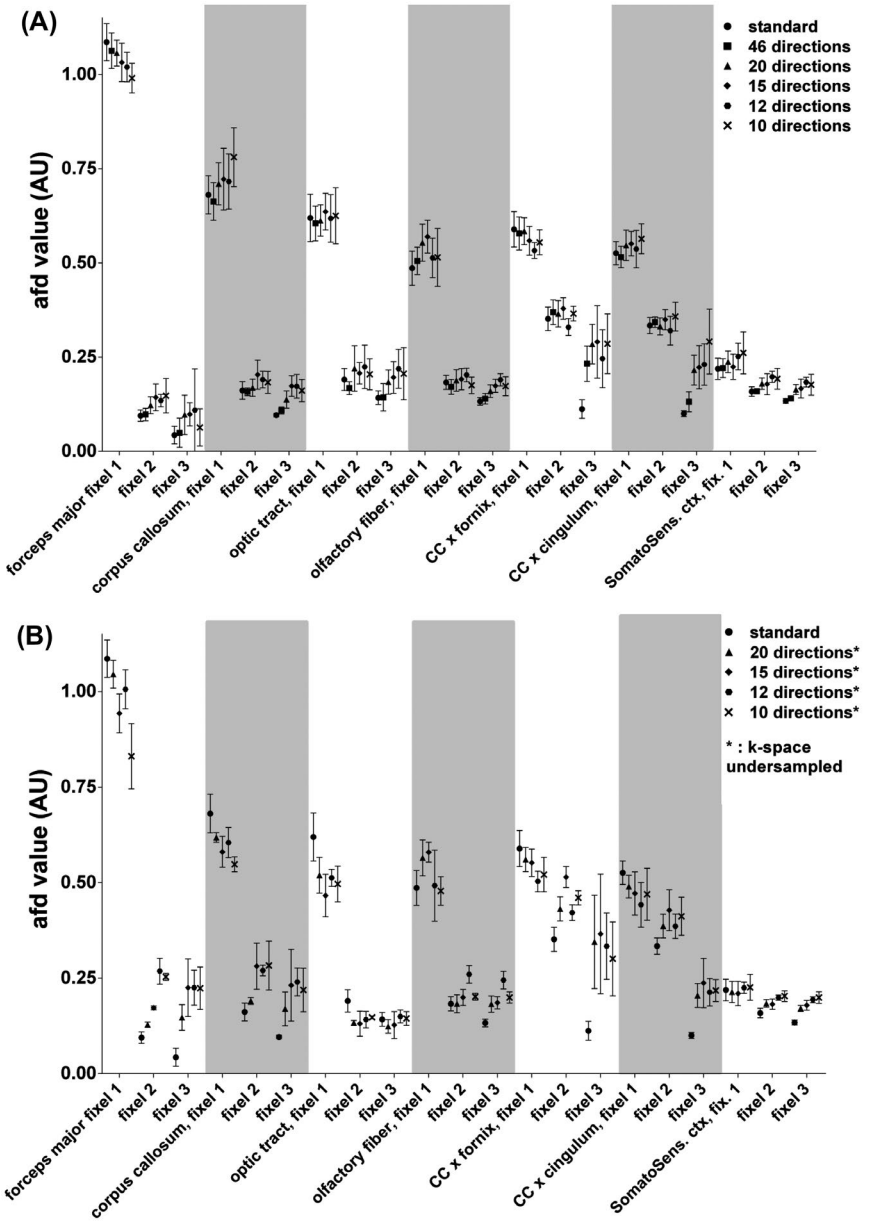

FIGURE 7 AFD values for the three most prominent fixels per ROI. A, For q-space undersampling ($n = 6$). B, For combined k-space and q-space undersampling ($n = 3$). Error bars indicate the SD between the animals. Single fiber ROIs should have a high AFD value in the primary voxel only, crossing fiber regions should still have a lower AFD value in the tertiary fixel, and the cortical ROI should have a low, isotropic AFD. The somatosensory cortex is abbreviated as SomatoSens. ctx in the legend

set during protocol optimization, there is no need for any additional steps during the acquisition itself. The blurring in Figure 6C,F is caused by the inefficient implementation of the undersampling. While undersampling only along the phase-encoded direction is technologically easy to implement and adapt,[70-72] it causes artifacts that are not entirely incoherent and are difficult to distinguish from real signal for the CS reconstruction algorithm. CS could be more successful if it was done in two dimensions using a more dedicated sequence, for example, by using a radial acquisition[73] or a PROPELLER acquisition.[74,75] In the case of undersampled k-space data, the CS reconstruction will simultaneously act as a denoiser. Shearlet-based denoising of DWIs has been investigated before.[76]

An alternative way for reducing the acquisition time is by using partial Fourier sampling, which can attain a speed-up factor similar to that presented here using CS, but partial Fourier sampling causes image degradation as well.[77] While CS offers more possibilities for further acceleration, for example, 2D subsampling or simultaneous k- and q-space reconstruction, partial Fourier sampling is a viable alternative to CS in k-space as it was applied in this research.

Due to time constraints during acquisition, data from 46 directions were resampled to 60 directions and used as a "standard" in this work. However, 60 directions are commonly acquired to improve the SNR of a 8th order CSD analysis, and such a full set of 60 directions was acquired for two animals. Supporting Information Figure S3 shows the AFD values found for a single animal using this "standard" scan, using the acquired 60 directions, and using the acquired 60 directions interpolated to the theoretical 60 directions. There is no effect of the interpolation on the AFD values. There is,

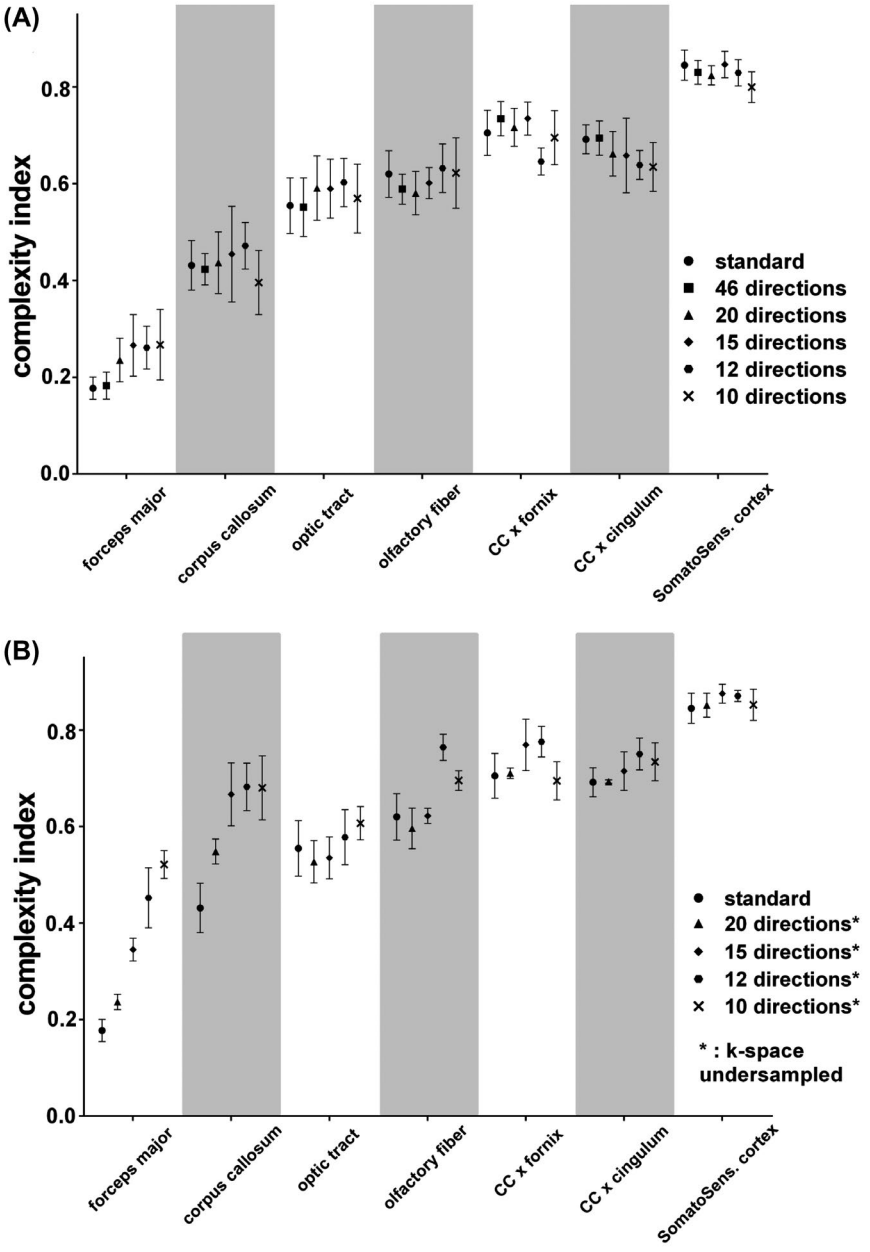

FIGURE 8 Complexity index values per ROI. A, For q-space undersampling ($n = 6$). B, For combined k-space and q-space undersampling ($n = 3$). Error bars indicate the SD between the animals. Single fiber regions should have a lower complexity as crossing fiber regions, which should have a lower index as the cortical ROI. The somatosensory cortex is abbreviated as SomatoSens. cortex in the legend

in general, a minor decrease of the AFD of the primary fixel, and a minor increase of the AFD values of spurious fixels when using 46 directions compared to 60 directions. Thus, while the overall SNR of the measurement using 46 directions is lower compared to 60 directions, it can act as a valid reference measurement.

Understanding the behavior of the AFD under different acquisition and reconstruction conditions is important since it can be used to derive several other quantitative measures.[38,39] The results from the phantom experiment indicate that when fewer directions are used, the CS reconstruction recognizes parts of the noise as signal, which results in the CSD algorithm finding a larger tertiary fixel. In crossing fiber regions, the primary fixel is less affected as the others, thus, explaining the decreasing complexity metric.

In the in vivo results, an increase of the AFD value of fixels without corresponding fibers is also observed. However, the primary fixel of the in vivo results are less affected by the undersampling of q-space, except for the forceps major, which is the strongest fiber and approaches the single fiber of the phantom best. The replicability of the measurement decreases, indicated here by the larger AFD SDfrom the animal group. Much like the b-value can influence the metrics acquired in DTI, here as well an effect of the acquisition strategy on the metrics is observed.

The reconstructions of the data that were also undersampled in k-space are of lower quality as those with only q-space undersampling, with higher complexity values and AFD values of secondary and tertiary fixels, and lower AFD values in primary fixels. The different effect of k-space subsampling between the phantom and the in

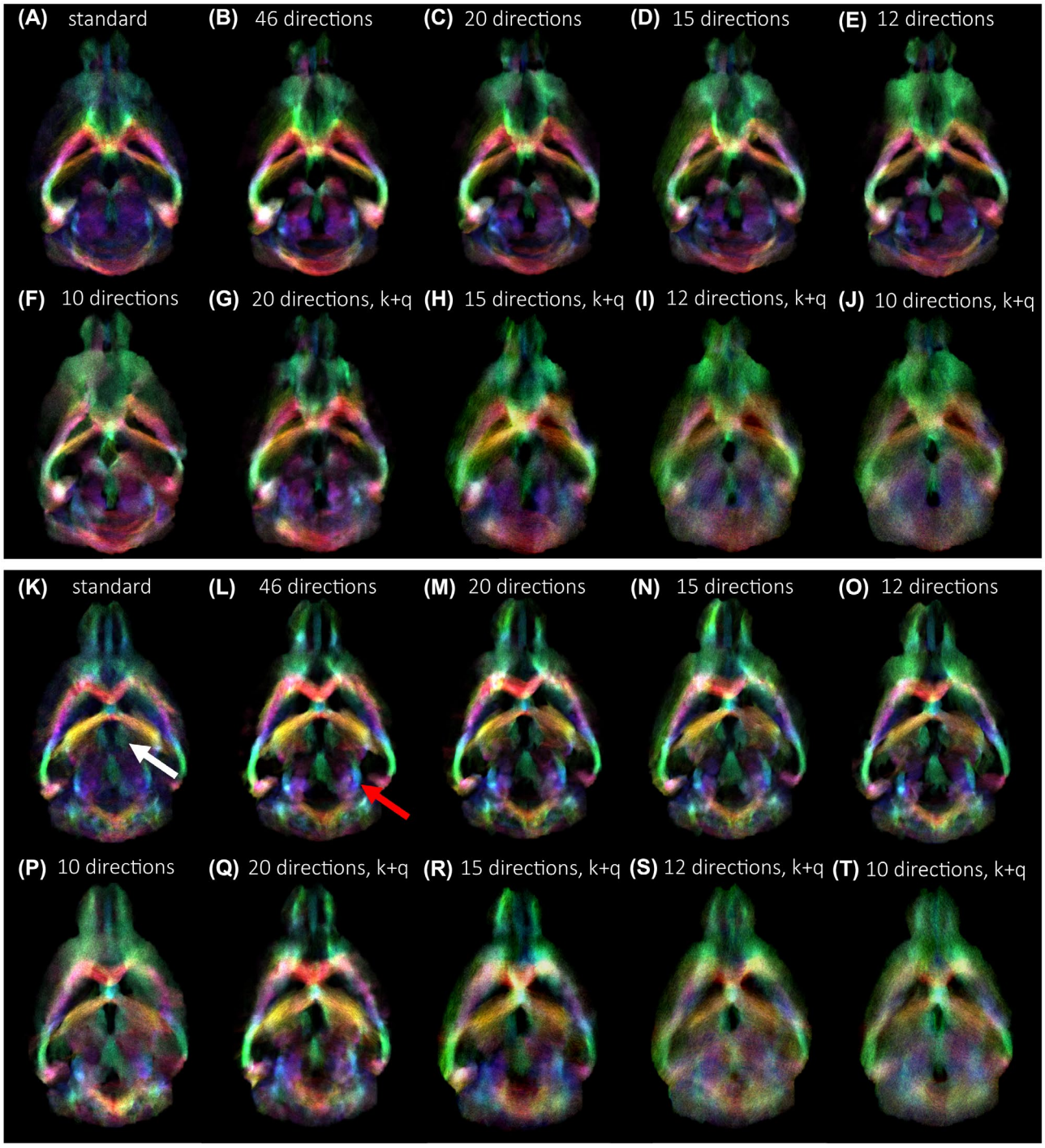

FIGURE 9 A-T, Representative slices of the tract density images, in a single animal. The number of diffusion volumes used is indicated above the image, with "k + q" indicating k-space undersampling was used as well

vivo acquisitions can be explained by the simple geometry of the phantom, which is ideally suited for CS. It should be noted that acquiring 15 diffusion directions with a full k-space takes about as long as acquiring 20 directions with an undersampled k-space. In this case, the full k-space sampling is a better strategy as undersampling k-space and acquiring more direction, both according to the quantitative values and according to the TDI results (Figure 9D,N vs G,Q, respectively). It is noteworthy that fewer spurious fibers are visible on the data using 46 dimensions with compressed sensing (Figure 9B,L) compared to the standard data (Figure 9A,K). This can be explained by the denoising properties of CS.

The results here indicate that FSE diffusion in combination with CS can be used to reduce the long acquisition time. The acquisition of 15 diffusion directions took just over 20 mi , about the same time as that of 60 directions with an EPI sequence.[42,43] As in the original paper presenting the spherical ridgelet-based

reconstruction of ODFs,[36] it was found that acquiring 15 to 20 directions allows for a reconstruction with an acceptable loss of information, both in the quantitative measures (AFD and complexity) and in the TDI images, thus, entirely removing the time penalty. Using fewer directions had the most obvious effect in the TDI images, where the quality became unacceptably low.

The method is applicable throughout the brain, as can be seen from the results of the ROI in the lower visual tracts, furthest from the coil and located lower as the amygdala, and the ROI in the olfactory bulb. Both the olfactory bulb and amygdala are very relevant in preclinical research, olfaction being the primary sense rodents depend on, while research involving the amygdala, which plays an important role in fear and stress, models, for example, post-traumatic stress disorder.[78] The olfactory bulb is also relevant in translational research to humans,[82] with its importance shown in neurodegenerative diseases, for example, Parkinson disease.[79-81] Experiments where diffusion imaging is applied to the olfactory bulb[83-85] or amygdala[78,86] are scarce, because of the difficulties in imaging it using an EPI sequence, with no examples of HARDI models being applied in mice yet.

Manganese enhanced MRI and volumetry have been used as quantitative measures instead,[87-92] but neither can be used to investigate brain wide structural connectivity, and manganese enhanced MRI is more invasive. fMRI has been applied in the amygdala,[93,94] and recently fMRI of the entire olfactory system has been achieved,[95] which would be complemented by the technique presented in this research. It should be noted that CSD is not well suited for investigating gray matter areas, but other techniques, such as listed in the Introduction section,[5-8,10] or a multi-shell multi-tissue analysis[96] would be more useful for such a purpose.

While CS was used here to speed up the FSE sequence, it could also be used in combination with an EPI sequence. Undersampling the q-space and reconstructing the ODFs using CS can be done simultaneously with multislice imaging[97] on clinical scanners, further reducing the acquisition time. The q-space CS technique used here was applied earlier in humans and validated in a numerical phantom.[36]

There are still shortcomings in this study. The sequence is limited to low ETL values, since part of the signal is rejected by the crushers, which are needed to correct the motion and FSE-induced phase errors. Using lower b-values and a higher bandwidth, this ETL could possibly be improved. The rejections of part of the signal also results in a low SNR of the diffusion weighted images, which is adequate but near the limit of what can be used for a meaningful analysis.[98] Cross terms between the imaging and diffusion gradients have not been taken into account, by either the reconstruction algorithm or MRtrix, which could have an influence on the AFD values.[99] The reconstruction using separate steps for reconstruction in k-space and q-space is still inelegant, and could be improved if an algorithm for the implementation of a simultaneous k- and q-space reconstruction was used. However, to our knowledge, such an algorithm does not yet exist except in the context of DSI,[100,101] where the accelerated acquisition would still take more time as with the method presented here. Preliminary results by the authors show that a similar approach to that of Golkov et al[102] might be feasible in our data, but several practical hurdles remain, such as the investigation and possible incorporation of the effects of motion, eddy currents, and cross-terms. A different possibility for tackling these problems in the future would be deep learning methods that work well with few q-space samples.[103-105]

While the 60 directions used in this study were ordered such that the q-space would be optimally covered by a given subset upon truncation, q-space undersampling was done using subsets of these 60 directions. As indicated by the results of the phantom experiment, calculating a dedicated q-space sampling scheme for the number of acquired direction could improve the q-space coverage, although it would not erase the effect of subsampling completely.

While the replicability was tested by repeating the experiment on several animals, a test-retest within the same animal was not done, as the protocol was too demanding to allow scanning the same animal twice in a short time frame.

5 | CONCLUSIONS

Preclinical DWI scans using the FSE sequence were acquired faster by using comCS, either in q-space only or in q-space and k-space simultaneously. The in vivo and phantom experiments show that using only q-space undersampling is useful for HARDI acquisitions using CSD, even when only 15 or 20 diffusion directions are used. However, additional undersampling in k-space in vivo has a detrimental effect on the measures, which can be explained by the fact that the implemented undersampling in k-space was performed only along a single dimension. The results from the in vivo experiment were replicable. This method can be used in preclinical research targeted at regions that are difficult to image using traditional EPI, such as the olfactory bulb or near the ear cavities. While tested for animals in this research, the same method could be used to speed up human FSE diffusion scans, or any EPI scan.

ACKNOWLEDGMENTS

We thank prof. Michailovich for sharing his code.[37] This work was supported by the interdisciplinary PhD grant (ID) UA BOF-DOCPRO 2012, the EU's Seventh Framework Programme (grant FP7/2007-2013; INMiND) [grant agreement 278850], the molecular Imaging of Brain

Pathophysiology (BRAINPATH) [grant FP7-PEOPLE-2013-IAPP-612360], by the Hercules stichting [grant agreement no. AUHA/012], HFSP RGP0006/201. None of the funding sources had any influence on the design or conduct of the study.

ORCID

Maarten Naeyaert https://orcid.org/0000-0002-7452-5534
Jan Aelterman https://orcid.org/0000-0002-5543-2631
Vladimir Golkov https://orcid.org/0000-0002-8665-1335
Daniel Cremers https://orcid.org/0000-0002-3079-7984
Aleksandra Pižurica https://orcid.org/0000-0002-9322-4999
Jan Sijbers https://orcid.org/0000-0003-4225-2487
Marleen Verhoye https://orcid.org/0000-0002-6267-0611

REFERENCES

1. Tournier JD, Calamante F, Gadian DG, Connelly A. Direct estimation of the fiber orientation density function from diffusion-weighted MRI data using spherical deconvolution. *Neuroimage*. 2004;23:1176-1185.
2. Tournier JD, Calamante F, Connelly A. Robust determination of the fibre orientation distribution in diffusion MRI: Non-negativity constrained super-resolved spherical deconvolution. *Neuroimage*. 2007;35:1459-1472.
3. Tuch DS. Q-ball imaging. *Magn Reson Med*. 2004;52:1358-1372.
4. Wedeen VJ, Hagmann P, Tseng WYI, Reese TG, Weisskoff RM. Mapping complex tissue architecture with diffusion spectrum magnetic resonance imaging. *Magn Reson Med*. 2005;54:1377-1386.
5. Zhang H, Schneider T, Wheeler-Kingshott CA, Alexander DC. NODDI: Practical in vivo neurite orientation dispersion and density imaging of the human brain. *Neuroimage*. 2012;61:1000-1016.
6. Assaf Y, Basser PJ. Composite hindered and restricted model of diffusion (CHARMED) MR imaging of the human brain. *Neuroimage*. 2005;27:48-58.
7. Palombo M, Ianus A, Guerreri M, et al. SANDI: A compartment-based model for non-invasive apparent soma and neurite imaging by diffusion MRI. *Neuroimage*. 2020;215:116835.
8. Lampinen B, Szczepankiewicz F, Mårtensson J, van Westen D, Sundgren PC, Nilsson M. Neurite density imaging versus imaging of microscopic anisotropy in diffusion MRI: A model comparison using spherical tensor encoding. *Neuroimage*. 2017;147:517-531.
9. Novikov DS, Kiselev VG, Jespersen SN. On modeling. *Magn Reson Med*. 2018;79:3172-3193.
10. Veraart J, Nunes D, Rudrapatna U, et al. Noninvasive quantification of axon radii using diffusion MRI. *Elife*. 2020;9.
11. Wedeen VJ, Wang RP, Schmahmann JD, et al. Diffusion spectrum magnetic resonance imaging (DSI) tractography of crossing fibers. *Neuroimage*. 2008;41:1267-1277.
12. Holland D, Kuperman JM, Dale AM. Efficient correction of inhomogeneous static magnetic field-induced distortion in Echo Planar Imaging. *Neuroimage*. 2010;50:175-183.
13. Hennig J, Nauerth A, Friedburg H. RARE imaging: A fast imaging method for clinical MR. *Magn Reson Med*. 1986;3:823-833.
14. Bastin ME, Le Roux P. On the application of a non-CPMG single-shot fast spin-echo sequence to diffusion tensor MRI of the human brain. *Magn Reson Med*. 2002;48:6-14.
15. Meiboom S, Gill D. Modified spin-echo method for measuring nuclear relaxation times. *Rev Sci Instrum*. 1958;29:688-691.
16. Mori S, Van ZPCM, van Zijl PCM. A motion correction scheme by twin-echo navigation for diffusion-weighted magnetic resonance imaging with multiple RF echo acquisition. *Magn Reson Med*. 1998;40:511-516.
17. Liu G, Van Gelderen P, Duyn J, Moonen CTW. Single-shot diffusion MRI of human brain on a conventional clinical instrument. *Magn Reson Med*. 1996;35:671-677.
18. Wan X, Parker DL, Lee JN, Buswell HR, Gullberg GT. Reduction of phase error ghosting artifacts in thin slice fast spin-echo imaging. *Magn Reson Med*. 1995;34:632-638.
19. Park S-W, Lee J-H, Ehara S, et al. Single shot fast spin echo diffusion-weighted MR imaging of the spine: Is it useful in differentiating malignant metastatic tumor infiltration from benign fracture edema? *Clin Imaging*. 2004;28:102-108.
20. Hirata K, Nakaura T, Okuaki T, et al. Comparison of the image quality of turbo spin echo- and echo-planar diffusion-weighted images of the oral cavity. *Medicine (Baltimore)*. 2018;97:e0447.
21. Debbins J, Karis J, Pipe J. Advantages of fast spin-echo diffusion weighted imaging in detecting small stroke lesions. *Proc Int Soc Magn Reson Med*. 2006;48:140. Debbins2006.pdf.
22. Blockx I, Van Camp N, Verhoye M, et al. Genotype specific age related changes in a transgenic rat model of Huntington's disease. *NeuroImage*. 2011;58:1006-1016.
23. Teh I, Lohezic M, Aksentijevic D, Schneider J. Accelerated fast spin echo diffusion spectrum imaging in the mouse heart ex-vivo. *J Cardiovasc Magn Reson*. 2013;15(Suppl 1):W6.
24. Miller KL, McNab JA, Jbabdi S, Douaud G. Diffusion tractography of post-mortem human brains: Optimization and comparison of spin echo and steady-state free precession techniques. *Neuroimage*. 2012;59:2284-2297.
25. Lustig M, Donoho D, Pauly JM. Sparse MRI: The application of compressed sensing for rapid MR imaging. *Magn Reson Med*. 2007;58:1182-1195.
26. Lustig M, Donoho D, Santos JM, Pauly JM. Compressed sensing MRI. *IEEE Signal Process Mag*. 2008;25:72-82.
27. Donoho D. Compressed sensing. *IEEE Trans Inf Theory*. 2006;52:1289-1306.
28. Mallat SG. A theory for multiresolution signal decomposition: The wavelet representation. *IEEE Trans Pattern Anal Mach Intell*. 1989;11:674-693.
29. Grgic S, Grgic M, Zovko-cihlar B. Performance analysis of image compression using wavelets—Industrial electronics. *IEEE T Ind Electron*. 2001;48:682-695.
30. Candès E, Demanet L, Donoho D, Ying L. Fast discrete curvelet transforms. *Multiscale Model Simul*. 2006;5:861-899.
31. Guo K, Labate D. Optimally sparse multidimensional representation using shearlets. *SIAM J Math Anal*. 2007;39:298-318.
32. Goossens B, Aelterman J, Luong H, Pižurica A, Philips W. Efficient design of a low redundant discrete shearlet transform. 2009 Int Work Local Non-Local Approx Image Process LNLA 2009. 2009:112-124.
33. Candès EJ, Romberg J, Tao T. Robust uncertainty principles: Exact signal reconstruction from highly incomplete frequency information. *IEEE Trans Inf Theory*. 2006;52:489-509.

34. Block KT, Uecker M, Frahm J. Undersampled radial MRI with multiple coils. Iterative image reconstruction using a total variation constraint. *Magn Reson Med*. 2007;57:1086-1098.
35. Michailovich O, Rathi Y. On approximation of orientation distributions by means of spherical ridgelets. *IEEE Trans Image Process*. 2010;19:461-477.
36. Michailovich O, Rathi Y, Dolui S. Spatially regularized compressed sensing of diffusion MRI data. *Psychiatry Interpers Biol Process*. 2010;1:1100-1115.
37. Michailovich O, Rathi Y, Dolui S. Spatially regularized compressed sensing for high angular resolution diffusion imaging. *IEEE Trans Med Imaging*. 2011;30:1100-1115.
38. Raffelt DA, Tournier J-D, Smith RE, et al. Investigating white matter fibre density and morphology using fixel-based analysis. *Neuroimage*. 2017;144:58-73.
39. Raffelt DA, Smith RE, Ridgway GR, et al. Connectivity-based fixel enhancement: Whole-brain statistical analysis of diffusion MRI measures in the presence of crossing fibres. *Neuroimage*. 2015;117:40-55.
40. Malisch TW, Hedlund LW, Suddarth SA, Johnson GA. MR microscopy at 7.0 T: Effects of brain iron. *J Magn Reson Imaging*. 1991;1:301-305.
41. Pandit P, Qi Y, King KF, Johnson GA. Reduction of artifacts in T2-weighted PROPELLER in high-field preclinical imaging. *Magn Reson Med*. 2011;65:538-543.
42. Praet J, Manyakov NV, Muchene L, et al. Diffusion kurtosis imaging allows the early detection and longitudinal follow-up of amyloid-β-induced pathology. *Alzheimers Res Ther*. 2018;10:1.
43. Anckaerts C, Blockx I, Summer P, et al. Early functional connectivity deficits and progressive microstructural alterations in the TgF344-AD rat model of Alzheimer's disease: A longitudinal MRI study. *Neurobiol Dis*. 2019;124:93-107.
44. Raffelt D, Tournier J-D, Rose S, et al. Apparent fibre density: A novel measure for the analysis of diffusion-weighted magnetic resonance images. *Neuroimage*. 2012;59:3976-3994.
45. Riffert TW, Schreiber J, Anwander A, Knösche TR. Beyond fractional anisotropy: Extraction of bundle-specific structural metrics from crossing fiber models. *Neuroimage*. 2014;100:176-191.
46. Papadakis NG, Murrills CD, Hall LD, Huang CL-H, Adrian CT. Minimal gradient encoding for robust estimation of diffusion anisotropy. *Magn Reson Imaging*. 2000;18:671-679.
47. Jones DK, Horsfield MA, Simmons A. Optimal strategies for measuring diffusion in anisotropic systems by magnetic resonance imaging. *Magn Reson Med*. 1999;42:515-525.
48. Tournier J-D, Smith R, Raffelt D, et al. MRtrix3: A fast, flexible and open software framework for medical image processing and visualisation. *Neuroimage*. 2019;202:116137.
49. Ning L, Laun F, Gur Y, et al. Sparse reconstruction challenge for diffusion MRI: Validation on a physical phantom to determine which acquisition scheme and analysis method to use? *Med Image Anal*. 2015;26:316-331.
50. Naeyaert M, Aelterman J, Van Audekerke J, Verhoye M. Quality and stability of compressed sensing schemes in the fast spin echo sequence. In: Le Franc Y, Vanduffel W, Sijbers J, Prodanov D, eds. *Frontiers in Neuroinformatics: Conference Abstract: Imaging the Brain at Different Scales: How to Integrate Multi-Scale Structural Information?* Lausanne, Switzerland: Frontiers; 2013:pp. 27-43, vol. 4.
51. Naeyaert M, Aelterman J, Sijbers J, et al. On the influence of pseudo-random sampling schemes for compressed sensing on 2D Cartesian rare acquisitions. In: Proceedings of the 6th Annual Meeting of the ISMRM Benelux Chapter. Vol 25. Eindhoven; 2016:320810.
52. Pruessmann KP, Weiger M, Scheidegger MB, Boesiger P. SENSE: Sensitivity encoding for fast MRI. *Magn Reson Med*. 1999;42:952-962.
53. Aelterman J, Naeyaert M, Gutierrez S, et al. Automatic high-bandwidth calibration and reconstruction of arbitrarily sampled parallel MRI. *PLoS One*. 2014;9:e98937.
54. Aelterman J, Luong HQ, Goossens B, Pižurica A, Philips W. COMPASS: A joint framework for parallel imaging and compressive sensing in MRI. *Proc—Int Conf Image Process ICIP*. 2010;1653-1656.
55. Totenhagen JW, Lope-Piedrafita S, Borbon IA, Yoshimaru ES, Erickson RP, Trouard TP. In vivo assessment of neurodegeneration in niemann-pick type C mice by quantitative T2 mapping and diffusion tensor imaging. *J Magn Reson Imaging*. 2012;35:528-536.
56. Veraart J, Novikov DS, Christiaens D, Ades-aron B, Sijbers J, Fieremans E. Denoising of diffusion MRI using random matrix theory. *Neuroimage*. 2016;142:394-406.
57. Veraart J, Fieremans E, Novikov DS. Diffusion MRI noise mapping using random matrix theory. *Magn Reson Med*. 2016;76:1582-1593.
58. Jenkinson M, Beckmann CF, Behrens TEJ, Woolrich MW, Smith SM. FSL. *Neuroimage*. 2012;62:782-790.
59. Andersson JLRR, Sotiropoulos SN. An integrated approach to correction for off-resonance effects and subject movement in diffusion MR imaging. *Neuroimage*. 2016;125:1063-1078.
60. Andersson JLR, Graham MS, Zsoldos E, Sotiropoulos SN. Incorporating outlier detection and replacement into a non-parametric framework for movement and distortion correction of diffusion MR images. *Neuroimage*. 2016;141:556-572.
61. Bastiani M, Cottaar M, Fitzgibbon SP, et al. Automated quality control for within and between studies diffusion MRI data using a non-parametric framework for movement and distortion correction. *Neuroimage*. 2019;184:801-812.
62. Tustison NJ, Avants BB, Cook PA, et al. N4ITK: Improved N3 bias correction. *IEEE Trans Med Imaging*. 2010;29:1310-1320.
63. Avants BB, Tustison NJ, Song G, Cook PA, Klein A, Gee JC. A reproducible evaluation of ANTs similarity metric performance in brain image registration. *Neuroimage*. 2011;54:2033-2044.
64. Hansen PC. The L-curve and its use in the numerical treatment of inverse problems. *Advances in Computational Bioengineering*. 2000;4:119-142.
65. Tournier JD, Calamante F, Connelly A. Determination of the appropriate b value and number of gradient directions for high-angular-resolution diffusion-weighted imaging. *NMR Biomed*. 2013;26:1775-1786.
66. Franklin KBJ, Paxinos G. *The Mouse Brain in Stereotaxic Coordinates*. 3rd edn. Amsterdam, the Netherlands: Elsevier; 2008.
67. Raffelt D, Tournier JD, Fripp J, Crozier S, Connelly A, Salvado O. Symmetric diffeomorphic registration of fibre orientation distributions. *Neuroimage*. 2011;56:1171-1180.
68. Tournier J-D, Calamante F, Connelly A. Improved probabilistic streamlines tractography by 2nd order integration over fibre orientation distributions. In: Proceedings of the 19th International Society for Magnetic Resonance in Medicine. Vol 88. 2010, p. 1670.
69. Calamante F, Tournier JD, Jackson GD, Connelly A. Track-density imaging (TDI): Super-resolution white matter

imaging using whole-brain track-density mapping. *Neuroimage*. 2010;53:1233-1243.
70. Sharma SD, Fong CL, Tzung BS, Law M, Nayak KS. Clinical image quality assessment of accelerated magnetic resonance neuroimaging using compressed sensing. *Invest Radiol*. 2013;48:638-645.
71. Vasanawala SS, Alley MT, Hargreaves BA, Barth RA, Pauly JM, Lustig M. Improved pediatric MR imaging with compressed sensing. *Radiology*. 2010;256:607-616.
72. Trzasko JD, Bao Z, Manduca A, McGee KP, Bernstein MA. Sparsity and low-contrast object detectability. *Magn Reson Med*. 2012;67:1022-1032.
73. Sarlls JE, Pierpaoli C. Diffusion-weighted radial fast spin-echo for high-resolution diffusion tensor imaging at 3T. *Magn Reson Med*. 2008;60:270-276.
74. Pipe JG. Motion correction with PROPELLER MRI: Application to head motion and free-breathing cardiac imaging. *Magn Reson Med*. 1999;42:963-969.
75. Pipe JG, Farthing VG, Forbes KP. Multishot diffusion-weighted FSE using PROPELLER MRI. *Magn Reson Med*. 2002;47:42-52.
76. Zhang X, Lu BL, Ma Y, Xu X, Wei F, Xu W. Denoising diffusion tensor images with shearlet. *Int Conf Signal Process Proceedings, ICSP*. 2012;2:962-965.
77. McGibney G, Smith MR, Nichols ST, Crawley A. Quantitative evaluation of several partial Fourier reconstruction algorithms used in MRI. *Magn Reson Med*. 1993;30:51-59.
78. Delgado y Palacios R, Verhoye M, Henningsen K, Wiborg O, Van der Linden A. Diffusion kurtosis imaging and high-resolution MRI demonstrate structural aberrations of caudate putamen and amygdala after chronic mild stress. Chen H, ed. *PLoS One*. 2014;9:e95077.
79. Georgiopoulos C, Warntjes M, Dizdar N, et al. Olfactory impairment in Parkinson's disease studied with diffusion tensor and magnetization transfer imaging. *J Parkinsons Dis*. 2017;7:301-311.
80. Skorpil M, Söderlund V, Sundin A, Svenningsson P. MRI diffusion in Parkinson's disease: Using the technique's inherent directional information to study the olfactory bulb and substantia Nigra. *J Parkinsons Dis*. 2012;2:171-180.
81. Rolheiser TM, Fulton HG, Good KP, et al. Diffusion tensor imaging and olfactory identification testing in early-stage Parkinson's disease. *J Neurol*. 2011;258:1254-1260.
82. Taha T, Megahed AA, Taha MS, Mahmoud H, Rabie TM, Askora AM. Diffusion tensor imaging: a smart move to olfactory pathway imaging; comparative study of chronic sinonasal polyposis patients and normal control. *Egyptian J Radiol Nucl Med*. 2020;51:34.
83. Zhao XG, Hui ES, Chan KC, et al. Identifying rodent olfactory bulb structures with micro-DTI. *Conf Proc Annu Int Conf IEEE Eng Med Biol Soc IEEE Eng Med Biol Soc Annu Conf*. 2008;2008:2028-2031.
84. Gutman DA, Magnuson M, Majeed W, et al. Mapping of the mouse olfactory system with manganese-enhanced magnetic resonance imaging and diffusion tensor imaging. *Brain Struct Funct*. 2013;218:527-537.
85. Rumple A, McMurray M, Johns J, et al. 3-dimensional diffusion tensor imaging (DTI) atlas of the rat brain. *PLoS One*. 2013;8:e67334.
86. Ding AY, Li Q, Zhou IY, et al. MR diffusion tensor imaging detects rapid microstructural changes in amygdala and hippocampus following fear conditioning in mice. Borchelt DR, ed. *PLoS One*. 2013;8:e51704.
87. Boretius S, Michaelis T, Tammer R, Ashery-Padan R, Frahm J, Stoykova A. In vivo MRI of altered brain anatomy and fiber connectivity in adult pax6 deficient mice. *Cereb Cortex*. 2009;19:2838-2847.
88. Saar G, Cheng N, Belluscio L, Koretsky AP. Laminar specific detection of APP induced neurodegeneration and recovery using MEMRI in an olfactory based Alzheimer's disease mouse model. *Neuroimage*. 2015;118:183-192.
89. Chuang K-H, Belluscio L, Koretsky AP. In vivo detection of individual glomeruli in the rodent olfactory bulb using manganese enhanced MRI. *Neuroimage*. 2010;49:1350-1356.
90. Pautler RG, Mongeau R, Jacobs RE. In vivo trans-synaptic tract tracing from the murine striatum and amygdala utilizing manganese enhanced MRI (MEMRI). *Magn Reson Med*. 2003;50:33-39.
91. Arimura D, Shinohara K, Takahashi Y, et al. Primary role of the amygdala in spontaneous inflammatory pain- Associated activation of pain networks—A chemogenetic manganese-enhanced MRI approach. *Front Neural Circuits*. 2019;13:58
92. Uselman TW, Barto DR, Jacobs RE, Bearer EL. Evolution of brain-wide activity in the awake behaving mouse after acute fear by longitudinal manganese-enhanced MRI. *Neuroimage*. 2020;116975.
93. Johnson FK, Delpech J-C, Thompson GJ, et al. Amygdala hyper-connectivity in a mouse model of unpredictable early life stress. *Transl Psychiatry*. 2018;8:49.
94. Harris AP, Lennen RJ, Marshall I, et al. Imaging learned fear circuitry in awake mice using fMRI. *Eur J Neurosci*. 2015;42:2125-2134.
95. Muir ER, Biju KC, Cong L, et al. Functional MRI of the mouse olfactory system. *Neurosci Lett*. 2019;704:57-61.
96. Jeurissen B, Tournier JD, Dhollander T, Connelly A, Sijbers J. Multi-tissue constrained spherical deconvolution for improved analysis of multi-shell diffusion MRI data. *Neuroimage*. 2014;103:411-426.
97. Barth M, Breuer F, Koopmans PJ, Norris DG, Poser BA. Simultaneous multislice (SMS) imaging techniques. *Magn Reson Med*. 2016;75:63-81.
98. Jones DK, Knösche TR, Turner R. White matter integrity, fiber count, and other fallacies: The do's and don'ts of diffusion MRI. *Neuroimage*. 2013;73:239-254.
99. Nair G, Hu XP. Manifestation and post hoc correction of gradient cross-term artifacts in DTI. *Magn Reson Imaging*. 2012;30:764-773.
100. Cheng J, Shen D, Basser PJ, Yap PT. Joint 6D k-q space compressed sensing for accelerated high angular resolution diffusion MRI. *Lect Notes Comput Sci (including Subser Lect Notes Artif Intell Lect Notes Bioinformatics)*. 2015;9123:782-793.
101. Sun J, Entezari A, Vemuri BC. Exploiting structural redundancy in q-space for improved EAP reconstruction from highly undersampled (k, q)-space in DMRI. *Med Image Anal*. 2019;54:122-137.
102. Golkov V, Portegies JM, Golkov A, Duits R, Cremers D. Holistic image reconstruction for diffusion MRI. In: Fuster A, Ghosh A, Kaden E, Rathi Y, Reisert M, eds. *Computational Diffusion MRI. Mathematics and Visualization*. Cham, Switzerland: Springer; 2016:pp. 27-39.
103. Golkov V, Dosovitskiy A, Sperl JI, et al. q-space deep learning: Twelve-fold shorter and model-free diffusion MRI scans. *IEEE Trans Med Imaging*. 2016;35:1344-1351.

104. Golkov V, Vasilev A, Pasa F, et al. q-space novelty detection in short diffusion MRI scans of multiple sclerosis. In: Proceedings of the 26th Annual Meeting of the International Society for Magnetic Resonance in Medicine. 2018, p. 5378. https://index.mirasmart.com/ISMRM2018/PDFfiles/5378.html
105. Swazinna P, Golkov V, Lipp I, et al. Negative-unlabeled learning for diffusion MRI. In: Proceedings of the 27th Annual Meeting of the International Society for Magnetic Resonance in Medicine. 2019, p. 3480.

SUPPORTING INFORMATION

Additional Supporting Information may be found online in the Supporting Information section.

FIGURE S1 Results for all sampling strategies in the phantom, for different SNR levels. The AFD per fixel is shown for A, a straight fiber, B, a curved fiber, C, two straight fibers crossing at 90°, D, a curved and straight fiber crossing. E, The complexity metric for all four ROI's. Error bars indicate the standard deviation over the ROI. A higher SNR generally results in a larger standard deviation, and very low AFD values become larger, although the mean of AFD values above the noise floor remains unaffected

FIGURE S2 Representative slices of the tract density images, in a single animal. The top half shows the brain at the level of the anterior commissure (white arrow), while the lower half shows the caudate putamen (red arrow). The number of diffusion volumes used is indicated above the image, with "k + q" indicating k-space undersampling was used as well

FIGURE S3 The effect of using 46 directions vs 60 directions, and the effect of interpolation in q-space: the results of the ROI analysis for a single animal, using the 60 directions as they were acquired and affected by motion (squares), after interpolating the acquired directions back to the theoretical directions (triangles), and using only 46 directions interpolated to 60 directions without applying CS regularization (circles)

How to cite this article: Naeyaert M, Aelterman J, Van Audekerke J, et al. Accelerating in vivo fast spin echo high angular resolution diffusion imaging with an isotropic resolution in mice through compressed sensing. *Magn Reson Med*. 2020;00:1–17. https://doi.org/10.1002/mrm.28520